Journal of Materials Chemistry A

PAPER

View Article Online
View Journal | View Issue

Cite this: J. Mater. Chem. A, 2019, 7, 3624

Hollow capsules of doped carbon incorporating metal@metal sulfide and metal@metal oxide core–shell nanoparticles derived from metal–organic framework composites for efficient oxygen electrocatalysis†

Feng Guo,[ab] Hui Yang,*[b] Lingmei Liu,[c] Yu Han,[c] Abdullah M. Al-Enizi,[d] Ayman Nafady,[de] Paul E. Kruger,[f] Shane G. Telfer*[g] and Shengqian Ma*[b]

Durable and inexpensive catalysts for the reduction of molecular oxygen and evolution of oxygen from water are desirable for electrochemical applications. However, going beyond state-of-the-art catalysts that are based on expensive noble metals remains a major challenge. Recently, nanostructured composites of conductive carbons and earth-abundant metals or metal oxides have emerged as promising electrocatalysts. Herein, we report a versatile and inexpensive synthetic method for the production of metal@metal sulfide core–shell nanoparticles (metal = cobalt, nickel) embedded in the walls of sulfur- and/or nitrogen-doped hollow carbon capsules. Metal oxide nanoparticle shells were also generated as an alternative to the metal sulfide shells. The fabrication of these materials was achieved *via* the thermal decomposition of sacrificial metal–organic framework nanocrystals coated with a metal–tannic acid coordination polymer shell, which delivered zerovalent metal nanoparticles embedded in the walls of the nitrogen-doped hollow carbon capsules. Subsequent pyrolysis processing in the presence of thiourea produced the metal sulfide nanoparticle shell. Alternatively, an oxide shell was generated under oxidizing conditions. The supported metal@metal sulfide and metal@metal oxide core–shell nanoparticles proved to be excellent catalysts for the electrochemical reduction of oxygen and evolution of oxygen from water, and they were far superior to analogous zerovalent metal nanoparticles. The materials produced accordingly allow the elucidation of key structure–activity relationships, and these insights reveal promising next-generation catalysts for important electrochemical processes that are derived from earth-abundant components.

Received 21st November 2018
Accepted 23rd January 2019

DOI: 10.1039/c8ta11213d

rsc.li/materials-a

Introduction

Metal–organic frameworks (MOFs) have attracted wide-ranging interest because of their well-defined structures, tunable pore sizes, and chemical functionalities,[1,2] and these inherent attributes can be exploited by employing MOFs as precursors in the fabrication of porous carbon materials *via* pyrolysis.[3–9] The attractive functional properties of these materials primarily lie in their chemical components and porous geometrics. A highly desirable feature of these MOF-derived carbon materials is their discrete and hollow character, which leads to the formation of hollow carbon capsules (HCCs).[6,8,10–12] Such HCCs can encapsulate, support, and protect secondary materials such as nanoparticles, which are otherwise prone to sintering or aggregating in the absence of a support. Furthermore, heteroatom doping (*e.g.*, S, N, and P) in these porous materials has been demonstrated as an effective strategy for improving their activity in the aforementioned applications.[11–15] Bare catalysts of various materials such as metals, metal oxides, metal sulfide,

[a]Chongqing Key Laboratory of Inorganic Special Functional Materials, College of Chemistry and Chemical Engineering, Yangtze Normal University, 16 Juxian Rd, Fuling, ChongQing, 408100, China

[b]Department of Chemistry, University of South Florida, 4202 E. Fowler Avenue, Tampa, Florida 33620, USA. E-mail: huiy@mail.usf.edu; sqma@usf.edu

[c]Advanced Membranes and Porous Materials Center, Physical Sciences and Engineering Division, King Abdullah University of Science and Technology, Thuwal 23955-6900, Saudi Arabia

[d]Chemistry Department, College of Science, King Saud University, Riyadh, 11451, Saudi Arabia

[e]Chemistry Department, Faculty of Science, Sohag, 82524, Egypt

[f]MacDiarmid Institute for Advanced Materials and Nanotechnology, Department of Chemistry, University of Canterbury, Christchurch 8140, New Zealand

[g]MacDiarmid Institute for Advanced Materials and Nanotechnology, Institute of Fundamental Sciences, Massey University, Palmerston North 4442, New Zealand. E-mail: s.telfer@massey.ac.nz

† Electronic supplementary information (ESI) available. See DOI: 10.1039/c8ta11213d

metal carbides, or metal phosphide nanoparticles in the interior of the heteroatom-doped hollow carbon capsules, abbreviated as NP@X–HCC (X = N, S, and P), often display vastly improved catalytic activity compared to non-encapsulated catalysts.[8,10,11,16–19]

Composites of doped porous carbon and metals, metal oxides, or metal sulfide nanoparticles that are derived from MOFs are promising low-cost substitutes for Pt-based catalysts for electrochemical catalytic reactions.[6,8,11,15,16,20–23] To achieve this substitution with enhanced activity and stability, a few approaches for the synthesis of heteroatom-doped HCCs encapsulated with non-noble metal-based nanoparticle composites have been developed,[19,24] whereas synthetic routes for obtaining NPs supported on an X–HCC are still rare. Traditional synthetic methods for obtaining NP@HCC or NP@X–HCC composites often require the use of a hard template, such as SiO_2 nanoparticles.[25,26] In such cases, template removal frequently involves harsh treatment, such as exposure to strong acids or bases, which may be incompatible with the chemical structure and/or composition of the target material.

To meet the challenge of avoiding hard templates in the fabrication of hollow nanomaterials, herein, we sought to develop a new strategy for the synthesis of metal@metal oxide core–shell nanoparticles and metal@metal sulfide core–shell nanoparticles embedded in heteroatom-doped HCCs. Our methodology for achieving this is summarized in Scheme 1. Metal–organic framework nanocrystals are employed to define the shape and size for the hollow structure. We select zeolitic imidazolate framework (ZIF)[2] nanocrystals for this role because they are nitrogen-rich precursors that produce nitrogen-doped porous carbon materials on pyrolysis. Nitrogen doping confers significant benefits to carbon-supported electrocatalysts.[5,27] The deposition of a uniform layer of potassium–tannic acid around the ZIF crystals from the soluble precursors is depicted in Step I (Scheme 1). This produces a ZIF-8@M–TA (metal–tannic acid coordination polymer) composite material.[17,18] Owing to the ready exchange of the potassium ions in the potassium–tannic acid layer with other metal ions, a range of metal ions can be incorporated in the shell layer in the second step (Step II, Scheme 1). Pyrolysis of this ZIF-8@M–TA composite material is performed to produce nitrogen-doped hollow carbon capsules which support the metal nanoparticles (Step III, Scheme 1). In this view, the exterior of the metal nanoparticles can be derived by either of the following two approaches. First, we envisage that by heating in the presence of a sulfur source, the outer layer of the metal nanoparticles is converted to the corresponding metal sulfide to generate metal@metal sulfide core–shell nanoparticles supported on carbon capsules (Step IV, Scheme 1, abbreviated as M@MS_x@S/N–HCC). Although the supported metal sulfide nanoparticles are excellent electrocatalysts, their controlled synthesis is challenging.[28,29] Furthermore, metal@metal sulfide core–shell nanoparticles derived from earth-abundant transition metals are rare and have been seldom investigated for their electrocatalytic properties. The pyrolysis reaction in Step IV is also expected to incorporate sulfur dopants into the carbon support, which will exist with the nitrogen dopants included by Step III. This is attractive for numerous reasons.[13,30,31] First, doping by heteroatoms introduces active polar sites, which facilitate the adsorption of electroactive guests and increase the rates of their electrochemical reactions.[13,30–32] Furthermore, the asymmetric spin density of the heteroatoms can play a key role in the electrocatalytic processes and for determining the mesopore structure.[13,30,31] It is noteworthy that the electrocatalytic activity of carbon-based materials that feature *multiple* dopants is often observed to be superior to that of materials with fewer dopants.[13,30,31] It appears that the synergistic effects between the dopants often lead to superior catalysts. As an alternative to metal sulfide formation and S doping of the carbon support, the supported metal nanoparticles can also be transformed to metal@metal oxide core–shell particles *via* a controlled oxidation step (Step V, Scheme 1, abbreviated as M@MO_x@N–HCC). We target these materials to expand the versatility of our synthetic methodology as well as investigate their excellent performance as electrocatalysts[33] and in electrochemical devices.[34,35] Incorporating transition metal@metal oxide core–shell nanostructures into conductive nanostructured porous carbon materials ensures close contact between the components at either the nano- or micro-scale and is an effective path for the development of electrode materials with superior performances.[20,36,37] For instance, a nitrogen-doped carbon-supported Co@Co_3O_4 composite, synthesized by the thermolysis of MOF nanocrystals, acts as a bifunctional oxygen electrode.[36] In addition, the Co@Co_3O_4@C core–shell nanoparticles encapsulated *in situ* to form a highly ordered porous carbon

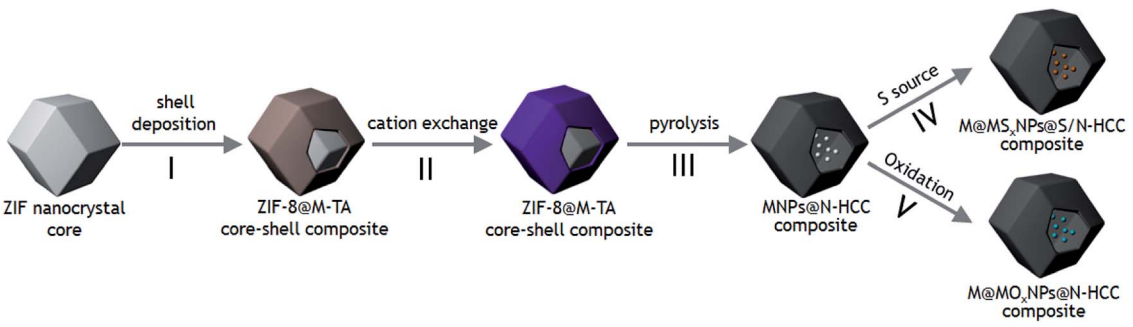

Scheme 1 Schematic of our strategy for using ZIF nanocrystals as sacrificial templates for the synthesis of composite materials comprising metal nanoparticles with metal sulfide or oxide shells embedded in hollow carbon capsules.

matrix showed excellent activity for the oxygen reduction reaction (ORR).[20] Similarly, porous carbons decorated with Ni@NiO core–shell nanoparticles have been developed as high-performance supercapacitor electrodes.[37]

Results and discussion

The initial step of our synthetic methodology is to prepare the ZIF (ZIF-8, $[Zn(2\text{-methylimidazolate})_2]_n$) nanocrystals *via* an established synthetic route.[38] A potassium–tannic acid (K–TA) coordination polymer was subsequently deposited on the surface of the ZIF-8 nanocrystals to obtain the ZIF-8@K–TA composite.[17] Replacement of the potassium cations in the K–TA shell by Co(II) was achieved by simply dispersing and stirring the ZIF-8@K–TA nanocrystals in a methanolic solution of $Co(NO_3)_2$ for 120 min. Pyrolysis of ZIF-8@Co–TA at 900 °C produces Co@N–HCC composites, which consist of cobalt nanoparticles (CoNPs) with an average diameter of approximately 6.1 nm embedded in the carbon walls of the hollow capsules (Fig. 1a, S9 and S20†). At such high temperatures, the powder X-ray diffraction (PXRD) patterns show that the CoNPs adopt the fcc lattice structure (Fig. S3†). The Zn(II) ions of the ZIF-8 are reduced to Zn metal, which vaporizes and escapes from the material.[14,17]

Our next step was to investigate the incorporation of sulfur into both the metal nanoparticle and carbon support (Step IV, Scheme 1). To achieve this, we focused on high-temperature pyrolysis reactions of sulfur sources and Co@N–HCC. The most successful outcome was achieved by the inclusion of thiourea in the pores of Co@N–HCC, followed by calcination at 900 °C, which delivered $Co@CoS_2$@S/N–HCC. The materials obtained after the thiourea treatment and calcination displayed the same overall morphology as their Co@N–HCC precursors (Fig. S11†). The PXRD pattern of $Co@CoS_2$@S/N–HCC exhibited diffraction peaks associated with graphitic carbon,[14,36] fcc-Co, and CoS_2 (Fig. 2a). This indicates the presence of both metallic Co and CoS_2. To determine whether these components were present as separate entities or integrated, as envisaged, the core–shell nanoparticles were analyzed with high-angle annular dark-field scanning transmission electron microscopy (HAADF-STEM, Fig. 1b). These microscopy images show HCCs with the nanoparticles uniformly deposited on the capsule walls. These nanoparticles are confirmed to have a $Co@CoS_2$ core–shell structure *via* high-resolution HAADF-STEM (Fig. 1c). Each nanoparticle comprises two domains with distinct lattice fringes, with *d* spacings of 0.204 nm (interior) and 0.276 nm (shell) in the core and shell, respectively. These fringes correspond to the (111) plane of Co and (200) plane of CoS_2, respectively. The average diameter of the $Co@CoS_2$NPs in this composite is ~7.7 nm (Fig. S20†), which is slightly larger than that of the CoNPs in Co@N–HCC, and is consistent with the incorporation of sulfur. No nanoparticles were observed on the outer surface of the carbon capsules or separate from the capsules. Energy dispersive X-ray spectrometry (EDS) elemental mapping of the capsules further shows that the Co atoms are dispersed uniformly throughout the core–shell nanoparticles,

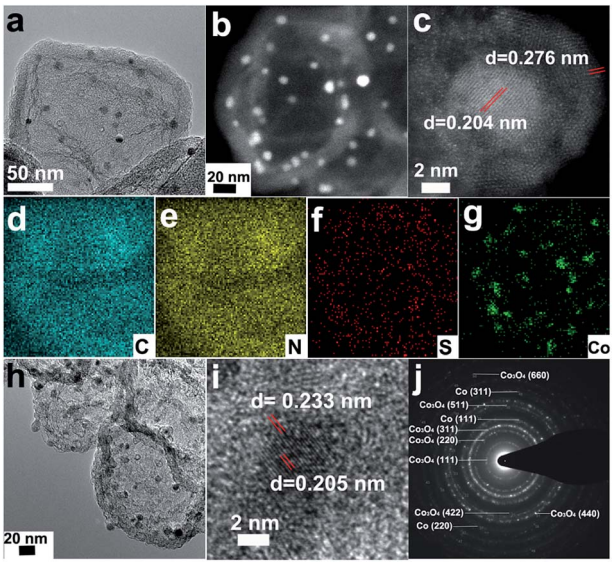

Fig. 1 (a) TEM image of Co@N–HCC; (b) HAADF-STEM image of $Co@CoS_2$@S/N–HCC; (c) High-resolution HAADF-STEM image showing an individual $Co@CoS_2$ core–shell nanoparticle; (d–g) EDS elemental (C, N, S, and Co) mapping of $Co@CoS_2$@S/N–HCC; (h) TEM image of $Co@Co_3O_4$@N–HCC; (i) HRTEM image showing an individual $Co@Co_3O_4$ core–shell nanoparticle; (j) SAED pattern of $Co@Co_3O_4$@N–HCC.

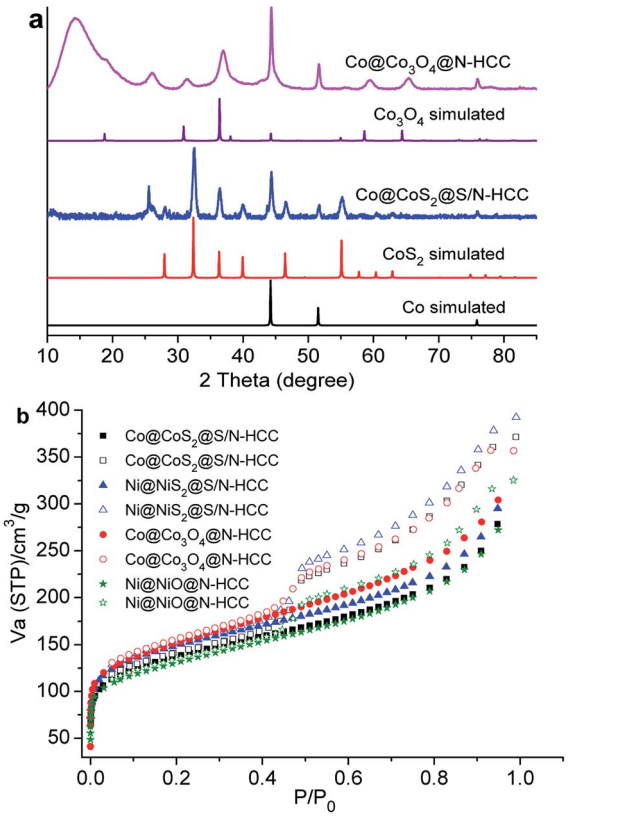

Fig. 2 (a) PXRD patterns of the as-synthesized materials; (b) N_2 adsorption (filled symbols) and desorption (open symbols) isotherms measured at 77 K for the as-synthesized materials.

whereas the N and S atoms are dispersed uniformly throughout the HCCs (Fig. 1d–g). The Co, N, and S contents of the Co@CoS_2@S/N–HCC composites were determined by inductively coupled plasma atomic emission spectroscopy (ICP-AES) and combustion elemental analysis (EA), and the values are listed in Table 1. The spectra obtained by X-ray photoelectron spectroscopy (XPS) analysis of Co@CoS_2@S/N–HCC also indicate the presence of cobalt, carbon, sulfur, and nitrogen. Three peaks can be seen in the C 1s region, which can be attributed to graphitic C (284.6 eV) and C–N and C–S groups (285.6 eV and 288.6 eV) (Fig. S27†). The N 1s spectra suggest the existence of N dopants in the carbon of the capsules, with three peaks corresponding to pyridine-like N (398.2 eV), pyrrole-like N (400.5 eV), and pyridine N–O-like (404.4 eV) moieties. The S doping is confirmed by the binding energies attributed to CS–Co (163.5 eV), C–S–C/C=S (164.4 eV), and C–SO_x–sulfate motifs (167.6 eV, 168.5, 169.2, and 169.7 eV).[39,40] The Co 2p spectrum was fitted to 780.9 and 796.7 eV and to 785.2 and 802.7 eV, corresponding to two spin–orbit doublets and two shake-up satellites, which are associated with the Co $2p_{3/2}$ and Co $2p_{1/2}$ levels, respectively.[41] The main binding energies are in close agreement with those previously reported for CoS_2 nanoparticles.[42] No metallic cobalt is detected, which may be ascribed to the shielding by the CoS_2 layer and carbon capsules.[17,43]

Based on the above findings, we decided to extend our methodology for the fabrication of hollow nanostructured composites of N–HCCs encapsulating Co@Co_3O_4 core–shell nanoparticles (Co@Co_3O_4@N–HCC). To this end, we heated Co@NHCC at 270 °C under air. This heating step maintained the nanostructural features of these materials, as shown by scanning electron microscopy (SEM) (Fig. S15†). The PXRD measurements conclusively show that the cobalt NPs are transformed to Co@Co_3O_4 core–shell NPs *via* the oxidation of their surface layers (Fig. 2). The transmission electron microscopy (TEM), high resolution (HRTEM), selected area electron diffraction (SAED), and XPS results show that the materials comprise Co@Co_3O_4 core–shell NPs of fairly uniform diameters (average ~ 9.1 nm) encapsulated within a nitrogen-doped hollow carbonaceous shell (Fig. 1h–j, S20 and S29†). The XPS spectra of Co@Co_3O_4@N–HCC show the presence of cobalt, carbon, oxygen, and nitrogen (Fig. S29†). The Co (2p) binding energies are in close agreement with those previously reported for Co@Co_3O_4 nanoparticles.[20,36]

Our synthetic methodology is also broadly applicable for the production of Ni@NiS_2@S/N–HCC and Ni@NiO@N–HCC by following the foregoing procedures. These materials have similar structures and morphologies as Co@CoS_2@S/N–HCC and Co@Co_3O_4@N–HCC (Fig. S4, S12, S16, and S19, S20†). Therefore, the synthetic methodology described here is a general method for the production of various metal@metal oxide and metal@metal sulfide core–shell nanoparticles encapsulated in heteroatom-doped HCCs.

N_2 gas sorption isotherms of Co@CoS_2@S/N–HCC, Ni@NiS_2@S/N–HCC, Co@Co_3O_4@N–HCC, and Ni@NiO@N–HCC were measured at 77 K. The isotherms of these materials exhibit a sharp uptake of N_2 at a low relative pressure ($P/P_0 < 0.1$) and a hysteresis loop at higher relative pressure ($0.4 < P/P_0 < 0.95$), indicating the existence of both micro- and meso-pores (Fig. 2). The calculated BET (Brunauer–Emmett–Teller) surface areas of these materials fall in the range 450–535 $m^2\ g^{-1}$ (Table S1†), whereas their total pore volumes are between 0.43 and 0.47 $cm^3\ g^{-1}$. The pore size distributions calculated from the experimental isotherms based on a DFT model confirm a hierarchical pore structure with the void diameters predominantly distributed around 20 Å, 35 Å, and 55 Å (Fig. S24, S25†). Such textural properties of these materials are anticipated to facilitate the accessibility of the active sites and promote substrate diffusion during the electrocatalytic processes.

Improvements in the catalysts used for the oxygen reduction reaction (ORR) and oxygen evolution reaction (OER) are highly sought[44] because they underlie the technological improvements in energy conversion devices such as regenerative fuel cells[45,46] and metal–air batteries.[47] For the ORR reaction, the state-of-the-art catalyst is Pt nanoparticles supported on an electrically conductive carbon.[48] Oxides of iridium and ruthenium are the most prominent electrocatalysts for the OER reaction.[49] However, these benchmark catalysts are rather expensive and suffer from stability issues at high anodic potentials, which precludes their adoption on a large scale. Using MOF-based materials as precursors has resulted in significant advances in this area.[28] In this light, the nanoparticles embedded in HCCs developed in this work have significant potential as electrocatalysts. The materials reported herein are fabricated using inexpensive components: zinc(II) and cobalt(II) or nickel(II) salts, thiourea or molecular oxygen, and 2-methylimidazole and tannic acid. Therefore, it is feasible to scale them up. To our

Table 1 Summary of the compositions and textural properties of the materials reported in this manuscript

Material	Precursor(s)	M[b] (wt%)	S (wt%)	N (wt%)	BET[c]	Pore[d] vol.
NC	ZIF-8	n/a[a]	n/a[a]	n/d[a]	821	0.45
NHCC	ZIF-8@K–TA	n/a[a]	n/a[a]	3.18	679	0.76
Co@N–HCC	ZIF-8@Co–TA	3.65	n/a[a]	4.50	512	0.58
Co@CoS_2@S/N–HCC	ZIF-8@Co–TA + thiourea	3.94	5.54	4.94	454	0.44
Co@Co_3O_4@N–HCC	ZIF-8@Co–TA + O_2	4.00	n/a[a]	4.55	535	0.47
Ni@N–HCC	ZIF-8@Ni–TA	3.13	n/a[a]	9.02	476	0.53
Ni@NiS_2@S/N–HCC	ZIF-8@Ni–TA + thiourea	4.38	4.26	7.49	489	0.46
Ni@NiO@N–HCC	ZIF-8@Ni–TA + O_2	3.96	n/a[a]	9.01	462	0.43

[a] n/a = not applicable; n/d = not determined. [b] M = Co or Ni; metal content determined by ICP-AES; other elements by elemental analysis. [c] BET surface area in $m^2\ g^{-1}$ determined by N_2 adsorption at 77 K. [d] Total pore volume in $cm^3\ g^{-1}$ determined by N_2 adsorption at 77 K.

knowledge, there are only few reports of core–shell nanoparticles with cobalt and an oxide shell.[20,36,50] Moreover, none of them use nickel, and there are no reports on nanoparticles with either these metals coated with sulfide shells.

To test these materials as ORR catalysts, we first performed cyclic voltammetry (CV) measurements using a conventional three-electrode electrochemical cell in O_2-saturated aqueous KOH solutions at room temperature (Fig. S32a†). A series of control reactions were also run using metal-free N-doped HCCs (N–HCC), N-doped carbon derived from the direct pyrolysis of ZIF-8 (NC), and commercial Pt/C. The results are summarized in Table 2. The CV curves display well-defined oxygen reduction peaks for all the materials, which disappear when the voltammograms are recorded in the absence of molecular oxygen.

The onset potential, half-wave potential, and ultimate current densities estimated from these measurements are listed in Table 2. These metrics are very similar to those of commercial Pt/C measured under identical conditions, and they are comparable with the best-performing materials reported in the literature (Table S1†). The lower onset and half-wave potentials recorded for the Co@N–HCCs highlight the advantages of generating sulfide or oxide shells around the embedded nanoparticles, which is easily enabled by our synthetic methodology. The limiting current densities of Co@CoS_2@S/N–HCC and Co@Co_3O_4@N–HCC are higher than that of Pt/C and many other reported non-precious metal catalysts (Fig. 3a, Table S1†). We then recorded linear sweep voltammograms (LSV) at different rotation speeds to generate the Koutecky–Levich plots of Co@CoS_2@S/N–HCC, Ni@NiS_2@S/N–HCC, Co@Co_3O_4@N–HCC, and Ni@NiO@N–HCC. These display good linearity and parallelism under different potentials (Fig. S32–S35†). This establishes that the reaction kinetics toward the dissolved oxygen are of the first order. The electron-transfer numbers are determined in the range from 0.4 to 0.7 V and found to fall between 3.8 and 3.9, which confirms that a four-electron pathway predominates and that H_2O_2 production is minimal. The reaction pathway was further probed using rotating ring disk electrode (RRDE) technique. Co@CoS_2@S/N–HCC shows n value higher than 3.7 in alkaline medium, with HO_2^- formation being lower than 3% over the whole range of potentials, thereby demonstrating its excellent electrocatalytic selectivity (Fig. S36†). The longevity and durability of all of the core–shell

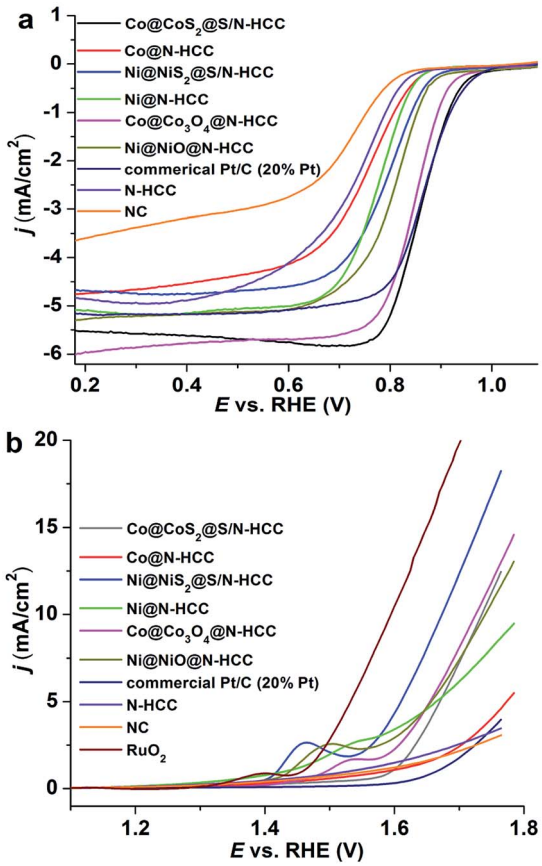

Fig. 3 (a) ORR and (b) OER polarization curves of different catalysts in O_2-saturated 0.1 M KOH solution (scan rate: 5 mV s^{-1}; rotation rate: 1600 rpm). Co@CoS_2@S/N–HCC and Ni@NiS_2@S/N–HCC exhibit the best ORR and OER performance, respectively. Commercial Pt/C and commercial RuO_2 are employed as ORR and OER standard catalysts, respectively. All potentials are given without *iR* correction.

Table 2 Summary of the ORR and OER electrocatalytic activities of the materials reported in this paper and those of commercially available catalysts

Material	ORR E_{onset} [b]	ORR E_{half} [c]	ORR $C_{density}$ [d]	OER E_{OER} η@10[e] mA cm^{-2}	OER Tafel slope[f]
NC	0.83	0.71	3.43	n/d[a]	n/d[a]
NHCC	0.86	0.73	4.94	n/d[a]	n/d[a]
Co@N–HCC	0.88	0.75	4.66	>1.8	233
Co@CoS_2@S/N–HCC	1.00	0.86	5.58	1.73	91
Co@Co_3O_4@N–HCC	0.96	0.84	5.86	1.72	161
Ni@N–HCC	0.88	0.77	5.17	>1.8	389
Ni@NiS_2@S/N–HCC	0.92	0.81	4.74	1.67	152
Ni@NiO@N–HCC	0.93	0.81	5.21	1.74	244
Commercial Pt/C (20% Pt)	1.01	0.85	5.17	n/d[a]	n/d[a]
RuO_2	n/a[a]	n/a[a]	n/a[a]	1.60	97

[a] n/a = not applicable; n/d = not determined. [b] ORR E_{onset} = the onset potential of electrocatalysis at a rotation speed of 1600 rpm in O_2-saturated 0.1 M KOH solution in V *vs.* RHE. [c] ORR E_{half} = the half-wave potential of the catalysts at a rotating speed of 1600 rpm in O_2-saturated 0.1 M KOH solution in V *vs.* RHE. [d] ORR $C_{density}$ = limiting current density at 0.3 V in mA cm^{-2}. [e] OER E_{OER} η@10 mA cm^{-2} = the potential of the catalysts at a current density of 10 mA cm^{-2} in V *vs.* RHE. [f] In mV dec^{-1}.

catalysts were retained after 16 h of CV cycle testing (Fig. S32–S35†). Chronoamperometric tests further confirmed the stability of Co@CoS_2@S/N–HCC (Fig. S36d†). Overall, these performance metrics place Co@CoS_2@S/N–HCC and Co@Co_3O_4@N–HCC in the top tier of oxygen reduction electrocatalysts.

The OER performance of the newly synthesized materials was evaluated in an O_2-saturated aqueous KOH solution (0.1 M). The LSV experiments exhibit that the potentials required to drive the current density to 10 mA cm^{-2} fall between 1.67 and 1.74 V (*vs.* RHE) for the catalysts with embedded metal and core–shell metal@metal sulfide/oxide nanoparticles (Fig. 3b, Table 2). For comparison, the benchmark material, RuO_2 exhibits a value of 1.60 V under the same experimental conditions. After 16 h of continuous CV cycling, the OER activity of these catalysts is undiminished (Fig. S38†). The OER activity of Ni@NiS_2@S/N–HCC (potential = 1.67 V) is the highest amongst the materials reported herein and is on par with other reported excellent non-precious metal catalysts such as Co–TA-800 (1.69 V),[51] Co@Co_3O_4/NC-1 (1.65 V),[36] and NGM (1.67 V)[52] (Table S2†). The cobalt and metal nanoparticles embedded in the carbon capsules, Co@N–HCC and Ni@N–HCC, are much poorer OER catalysts compared with their core–shell counterparts.

Conclusions

Nanocrystals of ZIF-8 are versatile sacrificial templates for the synthesis of doped hollow porous carbon capsules with embedded nanoparticles, which display high electrocatalytic activity. The exceptional electrocatalytic activity of the M@MS_x@S/N–HCC and M@MO_x@N–HCC composites can be ascribed to: (i) the electrical conductivity, porosity, and hollow morphology of the S/N–HCC and N–HCC capsules, which have excellent permeability and facilitate access of the substrates and electrons to the catalytic sites; (ii) firm attachment of the embedded nanoparticles to the carbon capsules to prevent sintering and dissociation and allow close contact with the conductive capsule walls; (iii) the presence of dopants (nitrogen and/or sulfur) in the carbon capsules, which are known to enhance the electrocatalytic activity;[13,31,53] and (iv) the presence of an oxide or sulfide shell on the surface of the metal nanoparticles to substantially elevate their electrocatalytic activity compared to the zerovalent metal precursors. The ability to selectively derive the surface of metal nanoparticles with sulfide or oxide layers while leaving other structural parameters unchanged, which is inherent to our synthetic methodology, enables the elucidation of catalytic structure–activity relationships. This is a crucial advantage of the strategy developed in this report because such comparisons of single variables are central to driving this research domain forward. The strategy presented here to fabricate these catalysts is straightforward and scalable, and we anticipate that it may be generalized to other heteroatom-doped hollow porous carbon capsules that support non-noble metal-based nanomaterial catalysts.

Experimental

The complete experimental details are provided in the ESI.†

Synthesis of ZIF-8@M–TA (M = K, Co, Ni)

In a typical synthesis, 200 mg of the ZIF-8 nanocrystals was dispersed in 10 mL of deionized water. Separately, a freshly prepared tannic acid solution (24 mM, 3 mL) was adjusted to pH 8 by the addition of aqueous KOH solution (6 M). Subsequently, the suspension of the ZIF-8 nanocrystals was added to the tannic acid solution. After stirring for 5 min, ZIF-8@K–TA was collected by centrifugation, washed several times with deionized water and methanol, and dried overnight under vacuum. The obtained ZIF-8@K–TA was soaked in a $Co(NO_3)_2 \cdot 6H_2O$/methanol (0.005 M, 30 mL) solution. After stirring for 120 min, ZIF-8@Co–TA was collected by centrifugation, washed several times with methanol, and finally dried overnight under vacuum. ZIF-8@Ni–TA was synthesized using a similar synthetic route, only changing $Co(NO_3)_2 \cdot 6H_2O$ to $Ni(NO_3)_2 \cdot 6H_2O$.

Synthesis of N–HCC and related M@N–HCC (M = Co, Ni) composites

ZIF-8@K–TA was transferred into a ceramic crucible, placed in a furnace under a dry nitrogen flow, and heated from 25 to 900 °C for 300 min. After reaching the target temperature, the sample was calcined for a further 3 h at 900 °C and then cooled to room temperature to obtain N–HCC. It was then washed several times with deionized water and methanol, and dried overnight under vacuum. Co@N–HCC, Ni@N–HCC, and NC were prepared similarly from the materials listed in Table 1.

Synthesis of Co@CoS_2@S/N–HCC and Ni@NiS_2@S/N–HCC composites

The as-synthesized Co@N–HCC composite was suspended in a mixture of absolute ethanol (35 mL) and deionized water (0.5 mL). Thiourea (1 g) was then added to the mixture. Subsequently, the temperature was increased to 85 °C under stirring. After 120 min, the solid was isolated by centrifugation and dried at 85 °C. The obtained sample was then transferred to a ceramic crucible, placed in a furnace under a dry nitrogen flow, and heated from room temperature to 900 °C over a period of 300 min. After reaching the target temperature, the sample was calcined for a further 0.5 h at 900 °C and then cooled to room temperature. The resulting solid product (named Co@CoS_2@S/N–HCC) was washed several times with benzene, deionized water, and ethanol; finally dried overnight; and collected for further use. Ni@NiS_2@S/N–HCC was synthesized using a similar synthetic route, only changing Co@N–HCC to Ni@N–HCC.

Synthesis of Co@Co_3O_4@N–HCC and Ni@NiO@N–HCC composites

The as-synthesized Co@N–HCC was transferred to a ceramic crucible, placed in a temperature-programmable furnace under a dry air flow, and heated from room temperature to 270 °C for 270 min. After reaching the target temperature, the sample was calcined for a further 5 h at 270 °C and then cooled to room temperature to yield Co@Co_3O_4@N–HCC. Ni@NiO@N–HCC

was synthesized using a similar synthetic route, only changing Co@N–HCC to Ni@N–HCC.

Electrochemical measurements

The ORR and OER tests were performed with a Pine electrochemical analyser (AFMSRCE Electrode Rotator WaveDriver 20 Bipotentiostat/Galvanostat System, USA) in an aqueous 0.1 M KOH electrolyte at room temperature. All the electrochemical measurements were conducted in a standard three-electrode system performed with a platinum counter electrode and Ag/AgCl (3.5 M KCl) reference electrode. A glassy carbon rotating disk electrode (RDE, 5.0 mm in diameter, 0.196 cm^2, Pine, USA) or rotating ring disk electrode (RRDE) supported the as-synthesized materials on the working electrode, with the rotation rate varying from 100 to 2200 rpm. Five milligrams of Co@CoS_2@S/N–HCC {or NC, N–HCC, Co@N–HCC, Ni@N–HCC, Ni@NiS_2@S/N–HCC, Co@Co_3O_4@N–HCC, Ni@NiO@N–HCC, Pt/C (20 wt% of Pt)} was dispersed in 1.1 mL of ethanol and 100 μL of deionized water (containing 100 μL of 5.0 wt% Nafion) solution under ultrasonic agitation to form an electrocatalyst ink. The ink was dropped on the surface of the pre-cleaned rotating disk working electrode and dried at room temperature. The catalyst loading was determined to be 0.1 mg cm^{-2}. Cyclic voltammograms were recorded in nitrogen (or oxygen)-saturated aqueous KOH (0.1 M) electrolyte at a scan rate of 20 mV s^{-1}. The linear sweep voltammetry curves were recorded at a scan rate of 5 mV s^{-1}. Commercial Pt/C (20 wt% of Pt) was employed for comparison. The oxygen evolution performance was tested using a method similar to that used for the ORR reaction. Commercial RuO_2 (loading ~0.8 mg cm^{-2}) was prepared as a catalyst using the same method for comparison.

Conflicts of interest

There are no conflicts to declare.

Acknowledgements

We acknowledge the financial support from University of South Florida. We extend our sincere appreciation to the Deanship of Scientific Research at King Saud University for funding this project through Research Group (RG #236) and RSSU for their technical support.

Notes and references

1 H.-C. Zhou, J. R. Long and O. M. Yaghi, *Chem. Rev.*, 2012, **112**, 673–674.
2 R. Banerjee, A. Phan, B. Wang, C. Knobler, H. Furukawa, M. O'Keeffe and O. M. Yaghi, *Science*, 2008, **319**, 939–943.
3 Q. Ren, H. Wang, X. F. Lu, Y. X. Tong and G. R. Li, *Adv. Sci.*, 2018, **5**, 1700515.
4 W. Xia, A. Mahmood, R. Zou and Q. Xu, *Energy Environ. Sci.*, 2015, **8**, 1837–1866.
5 Y. V. Kaneti, J. Tang, R. R. Salunkhe, X. Jiang, A. Yu, K. C. W. Wu and Y. Yamauchi, *Adv. Mater.*, 2017, **29**, 1604898.
6 L. Shang, H. Yu, X. Huang, T. Bian, R. Shi, Y. Zhao, G. I. N. Waterhouse, L.-Z. Wu, C.-H. Tung and T. Zhang, *Adv. Mater.*, 2016, **28**, 1668–1674.
7 H. Hu, J. Zhang, B. Guan and X. W. Lou, *Angew. Chem., Int. Ed.*, 2016, **55**, 9514–9518.
8 B. Y. Xia, Y. Yan, N. Li, H. B. Wu, X. W. Lou and X. Wang, *Nat. Energy*, 2016, **1**, 15006.
9 H. Zhang, H. Osgood, X. Xie, Y. Shao and G. Wu, *Nano Energy*, 2017, **31**, 331–350.
10 S. Choi, H. J. Lee and M. Oh, *Small*, 2016, **12**, 2425–2431.
11 X. Xu, F. Nosheen and X. Wang, *Chem. Mater.*, 2016, **28**, 6313–6320.
12 S. Yang, L. Peng, P. Huang, X. Wang, Y. Sun, C. Cao and W. Song, *Angew. Chem., Int. Ed.*, 2016, **55**, 4016–4020.
13 J.-S. Li, S.-L. Li, Y.-J. Tang, K. Li, L. Zhou, N. Kong, Y.-Q. Lan, J.-C. Bao and Z.-H. Dai, *Sci. Rep.*, 2014, **4**, 5130.
14 Y.-Z. Chen, C. Wang, Z.-Y. Wu, Y. Xiong, Q. Xu, S.-H. Yu and H.-L. Jiang, *Adv. Mater.*, 2015, **27**, 5010–5016.
15 P. Yin, T. Yao, Y. Wu, L. Zheng, Y. Lin, W. Liu, H. Ju, J. Zhu, X. Hong, Z. Deng, G. Zhou, S. Wei and Y. Li, *Angew. Chem., Int. Ed.*, 2016, **55**, 10800–10805.
16 S. Li, S. Peng, L. Huang, X. Cui, A. M. Al-Enizi and G. Zheng, *ACS Appl. Mater. Interfaces*, 2016, **8**, 20534–20539.
17 H. Yang, S. J. Bradley, A. Chan, G. I. N. Waterhouse, T. Nann, P. E. Kruger and S. G. Telfer, *J. Am. Chem. Soc.*, 2016, **138**, 11872–11881.
18 H. Yang, S. J. Bradley, X. Wu, A. Chan, G. I. N. Waterhouse, T. Nann, J. Zhang, P. E. Kruger, S. Ma and S. G. Telfer, *ACS Nano*, 2018, **12**, 4594–4604.
19 J. Liu, C. Wu, D. Xiao, P. Kopold, L. Gu, P. A. van Aken, J. Maier and Y. Yu, *Small*, 2016, **12**, 2354–2364.
20 W. Xia, R. Zou, L. An, D. Xia and S. Guo, *Energy Environ. Sci.*, 2015, **8**, 568–576.
21 Y. Li, B. Jia, Y. Fan, K. Zhu, G. Li and C.-Y. Su, *Adv. Eng. Mater.*, 2018, **8**, 1702048.
22 F. Lyu, Q. Wang, S. M. Choi and Y. Yin, *Small*, 2019, **15**, 1804201.
23 F. Lyu, Y. Bai, Z. Li, W. Xu, Q. Wang, J. Mao, L. Wang, X. Zhang and Y. Yin, *Adv. Funct. Mater.*, 2017, **27**, 1702324.
24 G. A. Ferrero, K. Preuss, A. Marinovic, A. B. Jorge, N. Mansor, D. J. L. Brett, A. B. Fuertes, M. Sevilla and M.-M. Titirici, *ACS Nano*, 2016, **10**, 5922–5932.
25 F. Bottger-Hiller, P. Kempe, G. Cox, A. Panchenko, N. Janssen, A. Petzold, T. Thurn-Albrecht, L. Borchardt, M. Rose, S. Kaskel, C. Georgi, H. Lang and S. Spange, *Angew. Chem., Int. Ed.*, 2013, **52**, 6088–6091.
26 R. Liu, S. M. Mahurin, C. Li, R. R. Unocic, J. C. Idrobo, H. Gao, S. J. Pennycook and S. Dai, *Angew. Chem., Int. Ed.*, 2011, **50**, 6799–6802.
27 Y. Nie, L. Li and Z. Wei, *Chem. Soc. Rev.*, 2015, **44**, 2168–2201.
28 A. Mahmood, W. Guo, H. Tabassum and R. Zou, *Adv. Eng. Mater.*, 2016, **6**, 1600423.
29 B. Chen, R. Li, G. Ma, X. Gou, Y. Zhu and Y. Xia, *Nanoscale*, 2015, **7**, 20674–20684.

30 J. Liang, Y. Jiao, M. Jaroniec and S. Z. Qiao, *Angew. Chem., Int. Ed.*, 2012, **51**, 11496–11500.
31 P. Chen, T. Zhou, L. Xing, K. Xu, Y. Tong, H. Xie, L. Zhang, W. Yan, W. Chu, C. Wu and Y. Xie, *Angew. Chem., Int. Ed.*, 2017, **56**, 610–614.
32 F. Lyu, Y. Bai, Q. Wang, L. Wang, X. Zhang and Y. Yin, *Materials Today Chemistry*, 2019, **11**, 112–118.
33 M. B. Gawande, A. Goswami, T. Asefa, H. Guo, A. V. Biradar, D.-L. Peng, R. Zboril and R. S. Varma, *Chem. Soc. Rev.*, 2015, **44**, 7540–7590.
34 L.-b. Jiang, X.-z. Yuan, J. Liang, J. Zhang, H. Wang and G.-m. Zeng, *J. Power Sources*, 2016, **331**, 408–425.
35 X. Xia, J. Tu, Y. Zhang, X. Wang, C. Gu, X.-b. Zhao and H. J. Fan, *ACS Nano*, 2012, **6**, 5531–5538.
36 A. Aijaz, J. Masa, C. Rösler, W. Xia, P. Weide, A. J. R. Botz, R. A. Fischer, W. Schuhmann and M. Muhler, *Angew. Chem., Int. Ed.*, 2016, **55**, 4087–4091.
37 Z. Zhang, Y. He, Q. Zhou, C. Huang, X. Zhang, Z. Guo, Y. Gao, J. Liu and Z. Cao, *Electrochim. Acta*, 2014, **144**, 300–306.
38 S. R. Venna, J. B. Jasinski and M. A. Carreon, *J. Am. Chem. Soc.*, 2010, **132**, 18030–18033.
39 D. Sun, R. Ban, P.-H. Zhang, G.-H. Wu, J.-R. Zhang and J.-J. Zhu, *Carbon*, 2013, **64**, 424–434.
40 Q. Wang, L. Jiao, H. Du, Y. Si, Y. Wang and H. Yuan, *J. Mater. Chem.*, 2012, **22**, 21387–21391.
41 H. van der Heide, R. Hemmel, C. F. van Bruggen and C. Haas, *J. Solid State Chem.*, 1980, **33**, 17–25.
42 H. Chen, J. Jiang, Y. Zhao, L. Zhang, D. Guo and D. Xia, *J. Mater. Chem. A*, 2015, **3**, 428–437.
43 G. H. Wang, J. Hilgert, F. H. Richter, F. Wang, H. J. Bongard, B. Spliethoff, C. Weidenthaler and F. Schuth, *Nat. Mater.*, 2014, **13**, 293–300.
44 Z. W. Seh, J. Kibsgaard, C. F. Dickens, I. Chorkendorff, J. K. Nørskov and T. F. Jaramillo, *Science*, 2017, 355.
45 W. Wang, F. Lv, B. Lei, S. Wan, M. Luo and S. Guo, *Adv. Mater.*, 2016, **28**, 10117–10141.
46 S. Li, C. Cheng and A. Thomas, *Adv. Mater.*, 2017, **29**, 1602547.
47 Z.-L. Wang, D. Xu, J.-J. Xu and X.-B. Zhang, *Chem. Soc. Rev.*, 2014, **43**, 7746–7786.
48 H. Mistry, A. S. Varela, S. Kühl, P. Strasser and B. R. Cuenya, *Nat. Rev. Mater.*, 2016, **1**, 16009.
49 N.-T. Suen, S.-F. Hung, Q. Quan, N. Zhang, Y.-J. Xu and H. M. Chen, *Chem. Soc. Rev.*, 2017, **46**, 337–365.
50 X. Liu, W. Liu, M. Ko, M. Park, M. G. Kim, P. Oh, S. Chae, S. Park, A. Casimir, G. Wu and J. Cho, *Adv. Funct. Mater.*, 2015, **25**, 5799–5808.
51 J. Wei, Y. Liang, Y. Hu, B. Kong, J. Zhang, Q. Gu, Y. Tong, X. Wang, S. P. Jiang and H. Wang, *Angew. Chem., Int. Ed.*, 2016, **55**, 12470–12474.
52 C. Tang, H.-F. Wang, X. Chen, B.-Q. Li, T.-Z. Hou, B. Zhang, Q. Zhang, M.-M. Titirici and F. Wei, *Adv. Mater.*, 2016, **28**, 6845–6851.
53 J.-C. Li, P.-X. Hou, S.-Y. Zhao, C. Liu, D.-M. Tang, M. Cheng, F. Zhang and H.-M. Cheng, *Energy Environ. Sci.*, 2016, **9**, 3079–3084.